Hybrid torque sensing concept for high frequency and dynamic torque ripple measurements for brushless dc motors

Johannes Stoß
Elektrotechnisches Institut (ETI)
Karlsruhe Institute of Technology (KIT)
Karlsruhe, Germany
johannes.stoss@kit.edu

Benedikt Schmitz-Rode
Elektrotechnisches Institut (ETI)
Karlsruhe Institute of Technology (KIT)
Karlsruhe, Germany
benedikt.schmitz-rode@kit.edu

Linus Niklaus
Elektrotechnisches Institut (ETI)
Karlsruhe Institute of Technology (KIT)
Karlsruhe, Germany
uhrwl@student.kit.edu

Dr.-Ing. Andreas Liske
Elektrotechnisches Institut (ETI)
Karlsruhe Institute of Technology (KIT)
Karlsruhe, Germany
andreas.liske@kit.edu

Prof. Dr.-Ing. Marc Hiller
Elektrotechnisches Institut (ETI)
Karlsruhe Institute of Technology (KIT)
Karlsruhe, Germany
marc.hiller@kit.edu

Abstract — **This paper presents unique hybrid torque sensing concept, based on a combination of acceleration and torsion sensors. The combination of both increases the bandwidth of a conventional torsion sensor by a factor of 20 and allows precise torque measurements up to 4 kHz.**

Keywords — sensor, test bench, brushless drive, measurement, modelling

I. INTRODUCTION

The torque ripple of permanent magnet synchronous machines (PMSM) is mainly caused by cogging torque, angular dependent flux-linkages and inductances [1]. They can lead to additional noise, vibrations and machine resonances [2]. Recently, various control algorithms for torque ripple reduction have been proposed [2, 3]. To assess the efficiency of these algorithms, precise torque sensing with a large bandwidth is mandatory.

State of the art torque measurement is done by sensors with a torsion shaft. The mechanical resonance frequency of the load and device under test (DUT) connected by the torsion shaft thereby limits the measurement range. It is typically below 200 Hz [4].

To extend the bandwidth, torque harmonics can be measured by evaluation of the angular acceleration on a rotary encoder or with the use of acceleration sensors [4, 5]. It should be noted that this requires to install an additional sensor to measure the low-frequency torque, as constant torques do not cause angular accelerations and therefore cannot be measured. The evaluation of the rotary encoder is limited by its resolution and torsional stiffness. In [4] a bandwidth of less than 800 Hz was achieved.

The usage of acceleration sensors offers higher bandwidth and sensitivity compared to the rotary encoder methods. In the sensor setup proposed in [4], the acceleration sensors are attached to the motor shaft. For this purpose, complex circuits for analysis of the sensor data in the rotating part and transfer to the non-rotating parts need to be mounted on the drive shaft. This significantly increases its inertia and reduces the torque measurement sensitivity which makes the method unsuitable for small brushless dc machines [4].

In this paper the testbench design is adapted, enhanced and simplified for the requirements of small brushless dc machines. This new design results in higher overall bandwidth of up to 4 kHz.

II. TESTBENCH DESIGN

The testbench shown in Fig. 1 and Fig. 2 combines two acceleration sensors, two angular encoders and one torsion sensor.

The DUT (parameters listed in Table II) is placed inside a housing. The housing is rotatably mounted by two ball bearings and connected to the testbench using a helix coupling with low stiffness. The low stiffness leads to a low first resonance frequency of the acceleration sensor setup (detailed description in III). Since the stator housing is rotatably mounted and can thus rotate against the external angle sensor in the *Kistler 4503B* torsion sensor, another angle sensor is placed inside the housing. This additional *iC-Haus MH8 12-bit* encoder is located on the A-shaft of the DUT (Fig. 1 - left), while the B-shaft is used to couple the DUT to the torsion sensor and load.

Outside the DUT rotor housing, the two *PCB 352B* acceleration sensors ($\alpha_{\max} = 50 \frac{\mathrm{m}}{\mathrm{s}^2}$ and $f_{\max} = 10$ kHz) are placed in opposite directions to separate angular acceleration from vibration [6]. Since the housing is fixed by the helix coupling, the sensor signals can be transmitted with cables. This reduces the complexity of the testbench while increasing the measurement range due to lower inertia. Low frequency torque is measured by the *Kistler 4503B* torsion sensor ($T_{\max} = 5$ Nm) including a 13 Bit angular encoder [7]. The encoder also allows determination of the load rotor angle.
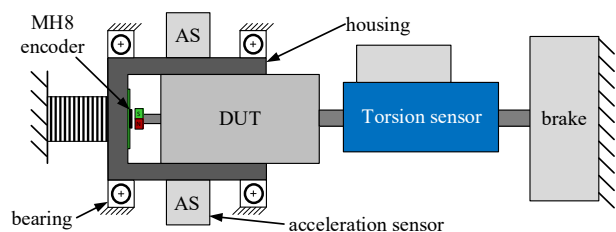
Fig. 1. Drawing of the proposed testbench design.

To reduce the influence of torque harmonics injected by the load, a *Magtrol HB-140M-2* hysteresis brake is used [8]. The hysteresis brake produces the load torque mainly by
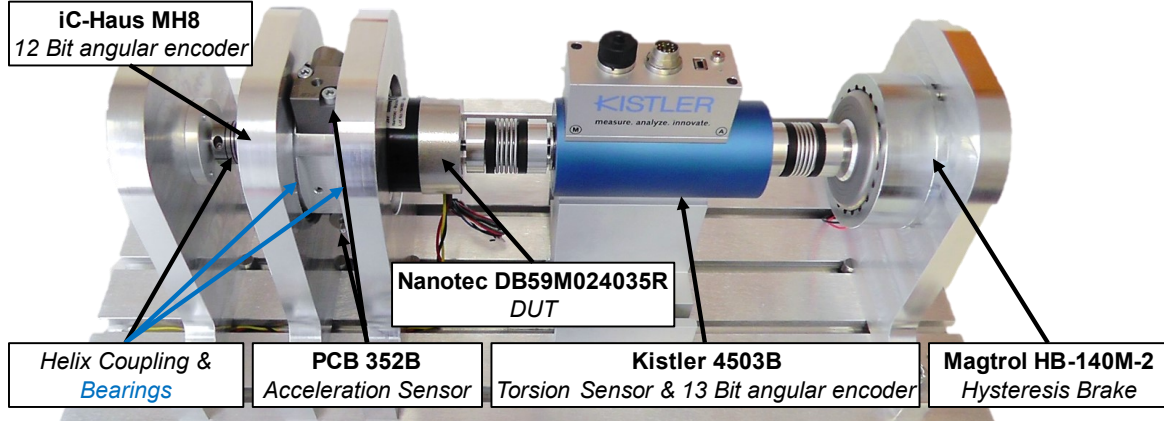
Fig. 2. Overview of the designed testbench.

hysteresis loss inside its rotor. Therefore, the torque has almost no speed dependence. Furthermore, the hysteresis brake has only negligible torque harmonics compared to a setup with a load machine. This enables an isolated observation of the torque harmonics of the DUT. Since the load only functions in breaking mode, the setup is limited to positive torque measurements on the DUT. For negative torque measurements a second brushless dc motor or induction motor must be mounted instead of the hysteresis brake.

III. ANALYTICAL EVALUATION

In this section, first torque measurement using torsion sensors and afterwards by acceleration sensors are examined individually under idealized conditions. At the end, the entire test stand is examined with the combination of both measuring principles.

The simplified equivalent model of a torsion sensor according to [4] is shown in Fig. 3. The inertia of the DUT rotor is J_R and J_B is the break inertia. The torsion sensor is modeled by a torsion spring. It is assumed that the bearing friction of the DUT and brake behave identical and only have a damping influence on the torque measuring shaft. Consequently, the total damping is assumed to be $2 \cdot \Gamma_{LP}$. The DUT torque is given by T_e. The transfer behavior is therefore similar to a double oscillator.
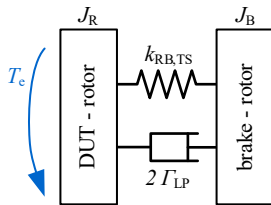
Fig. 3. Equivalent model of the torsion sensor measurement setup.

This can be described by its transfer function which is defined as the quotient of T_{TS} (torque measured by torsion sensor) and T_e (torque generated by DUT) [4]:

$$G_{TS} = \frac{T_{TS}}{T_e} \tag{3}$$

$$G_{TS} = \frac{2J_B\Gamma_{LP}s + J_B k_{RB,TS}}{J_B J_R s^2 + 2\Gamma_{LP}(J_B + J_R)s + k_{RB,TS}(J_B + J_R)} \tag{1}$$

Fig. 4 shows the transfer characteristics of the torsion sensor. As mentioned in the previous section, the torsion sensor only enables measurements up to the first resonance, which is mainly defined by the stiffness and inertias in the system (Table I). It can be calculated by:

$$f_{res,TS} = \frac{1}{2\pi}\sqrt{k_{RB,TS} \cdot \left(\frac{1}{J_B} + \frac{1}{J_R}\right)} \tag{2}$$

In this setup a resonance frequency of approx. 830 Hz is expected. This limits the linear region of the transfer function and thus also the sensor bandwidth to roughly 300 Hz. The bandwidth can be increased by reducing the inertias and increasing the stiffness. Since the torque is measured by the torsion angle of the sensor, lower torsion angles lead to reduced sensitivity. Therefore, the bandwidth of this measurement principle can only be increased with a reduction in measurement accuracy. The measuring principle is therefore unsuitable for measurement of torque harmonics, as these have high frequencies but only small amplitudes.
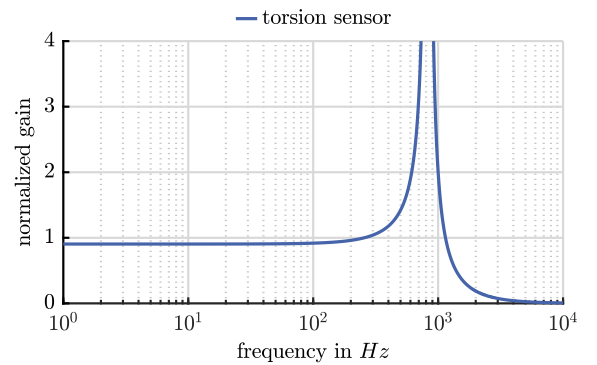
Fig. 4. Transfer behavior of the torsion sensor for the designed testbench. For better representation, the gain was normalized.

To overcome this limitation, the setup is extended by the acceleration sensor-based torque measurement with its equivalent model shown in Fig. 5.
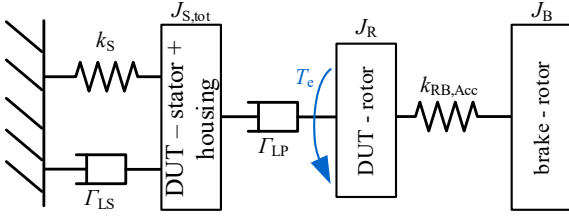
Fig. 5. Equivalent model of the acceleration sensor measurement setup.

For the purpose of describing the measuring principle, it is first assumed that the torque measurement is only carried out via the acceleration sensors and that the DUT is therefore directly connected to the load with no dedicated torque sensor. The characteristics of this connection are modelled by a torsion spring with the stiffness $k_{RB,Acc}$. Compared to the torsion sensor, the stiffness of the connection is thus significantly greater.

It is assumed that the bearing friction of the brake can be neglected. This approach is valid since the influence of the bearing friction of the brake is primarily visible at frequencies below the first resonance and thus outside the measuring range. The modelling of the bearing friction of the DUT, on the other hand, can contribute to the understanding of the system, as it leads to a transmission of the excitation at the resonance frequency of the DUT and brake to the acceleration sensor measurement system. This can also be seen in Fig. 6 at approx. 1.2 kHz.

The stator of the DUT is mounted inside the rotatable housing. Its total inertia is given by $J_{S,tot}$. The housing is rotatably mounted by two ball bearings and is held in place by the helix coupling. The mechanical properties of the ball bearings are modelled in a simplified way by the damping constant Γ_{LS}. The stiffness of the helix coupling (k_s) is chosen small to reduce the resonance frequency of the testbench. This is because the measuring range of the acceleration sensor setup is above the first resonance frequency, in contrast to the torsion sensor where the measuring range is limited by the first resonance.

The two non-rotating acceleration sensors are placed on the stator housing (Fig. 1 and Fig. 2). Since the angular acceleration is the second derivative of the angle, evaluation of the angular acceleration instead of the torsion angle reduces the number of integrator elements in the transfer function by two, compared to the torsion sensor. This allows measurements beyond the first resonance.

The transfer characteristic is given by:

$$G_{ACC} = \frac{\alpha_m}{T_e} \qquad (4)$$

$$G_{ACC} \qquad (5)$$
$$= \frac{s\left(J_B J_R s^3 + J_B \Gamma_{LP} s^2 + k_{RB,ACC} s(J_B + J_R) + k_{RB,ACC}\Gamma_{LP}\right)}{\left(J_B J_R s^2 + k_{RB,ACC}(J_B + J_R)\right)\left(J_{S,tot} s^2 + s(\Gamma_{LP} + \Gamma_{LS}) + k_S\right)}$$

By neglecting the bearing friction of the DUT (Γ_{LP}) the transfer function can be simplified to:

$$G_{ACC} = \frac{s^2}{J_{S,tot} s^2 + s\Gamma_{LS} + k_S} \qquad (6)$$

As previously outlined, the basic transmission characteristics can be described accurately by the simplification made in (6). However, the influence of the resonance between DUT and brake is neglected.

The frequency of the first resonance, which defines the start of the measurement range, is given by:

$$f_{res,ACC} = \frac{1}{2\pi}\sqrt{\frac{k_S}{J_{S,tot}}} \qquad (7)$$

α_m denotes the angular acceleration. To calculate the torque harmonics (T_{acc}), the acceleration is multiplied by the total stator inertia.

$$T_{acc} = \alpha_m \cdot J_{S,tot} \qquad (8)$$

Since the setup only outputs the acceleration of the two sensors, the angular acceleration must also be calculated from the tangential acceleration for a given radius R. To separate the tangential acceleration from vibration, the two sensors are mounted in opposite direction. By building the sum of the signals (α_{s1}, α_{s2}), the vibration can be eliminated.

$$\alpha_m = \frac{\alpha_{tan}}{R} = \frac{\alpha_{s1} + \alpha_{s2}}{2 \cdot R} \qquad (9)$$

Fig. 6 shows the ideal transfer characteristics of the rescaled torque T_{acc} of the acceleration sensor. As expected, the acceleration sensor setup achieves an almost flat response above the resonance frequency while the torsion sensor (Fig. 4) has a lowpass characteristic above its first resonance frequency.
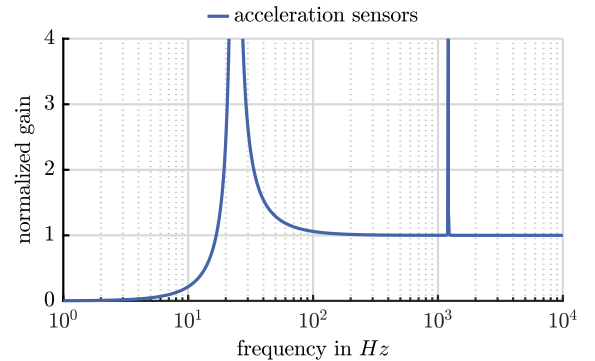
Fig. 6. Transfer behavior of the acceleration sensors for the designed testbench. For better representation the gain was normalized.

The resonance frequency can be adjusted through the stiffness of the helix coupling. In contrast to the torsion sensor, the first resonance frequency does not limit the measuring range upwards but downwards. This means that the detection of constant torques is not possible with acceleration sensors.

To enable torque measurement over the entire frequency range, the resonance frequency of the acceleration sensor measurement and thus the stiffness of the helix coupling must be selected to be small. In this setup, the first resonance frequency of the acceleration sensors is approx. 24 Hz. This means torques within the linear region of both transfer characteristics, between 200 Hz and 300 Hz, can be measured with both measurement principles (Fig. 4, Fig. 6). This enables a smooth transition between torsion sensor and acceleration sensor measurements.

TABLE I.   MECHANICAL DATA OF THE TESTBENCH

Symbol	Meaning	value
J_B	Inertia of break rotor	100 mg m^2
J_R	Inertia of DUT rotor	10.5 mg m^2
$J_{S,tot}$	Inertia of DUT stator + housing	1.305 g m^2
Γ_{LP}	Damping constant – rotor bearings	424 µ Nm s
$k_{RB,Acc}$	Total stiffness – acceleration sensor	549 Nm/rad
$k_{RB,TS}$	Total stiffness – torsion sensor	258 Nm/rad
k_S	Stiffness – helix coupling	29 Nm/rad
Γ_{LS}	Damping constant – DUT stator bearing	4.24 m Nm s

Considering the mass inertia of the couplings, the stiffness of the drive shafts and DUT itself, the total transfer function of the sensors can be estimated (Fig. 7). The upper limit of the measurement range is given by the self-resonance of the DUT stator. The self-resonance is determined by the structure of the DUT itself and can only be influenced to a small degree by the design of the test bench. By using a stiffer stator housing in the design of the DUT, the measuring range could theoretically be extended.
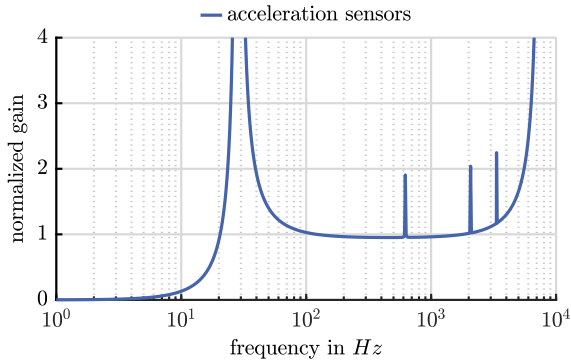
Fig. 7. Transfer behavior of the acceleration sensors including all testbench parts.

Using the basic characteristics of the testbench and the specifications of the acceleration sensors (*PCB 352B)* used, the theoretical minimum and maximum measurable torque harmonic amplitude can be estimated [6]:

$$T_{acc,min} = \frac{\alpha_{s1,min} \cdot J_{S,tot}}{R} = 21 \text{ µNm} \qquad (10)$$

$$T_{acc,max} = \frac{\alpha_{s1,max} \cdot J_{S,tot}}{R} = 97 \text{ mNm} \qquad (11)$$

Compared to torque measurement using a torsion sensor, only significantly smaller torques can be measured here. This design is valid because torque harmonics are typically minimized during machine design and are therefore only in the range of a few percent of the basic shaft torque. Since the torque scales with the inertia of the DUT and thus indirectly with the machine power and the torque, the measuring range is inevitably shifted to higher torques with this measuring principle. As larger machines are also expected to have higher amplitudes of the torque harmonics, this does not limit the measuring principle to small machines only.

IV. PMSM TORQUE RIPPLE MEASUREMENTS

To show the performance of the designed testbench, a campbell-diagram of the torsion and acceleration sensor as well as the analytically calculated inner torque is shown in Fig. 8. Therefore, a speed ramp from zero to 3200 rpm with $i_d = -4$ A and $i_q = 2$ A was performed. The current and speed were controlled by a cascaded PI control. The current control was performed on the real time processing system described in [9]. The power converter and the measuring equipment used are described in [10]. All measured variables were captured using a 16-bit AD converter with a sample rate of 5 MSPS. Subsequently, an average value was calculated over a control period of 50 µs. The controller and switching frequency were chosen to 20 kHz.

The calculated torque is based on identified angle-dependent flux linkages ψ using the method proposed in [3]. Since saturation is not present in most operating points the linear machine parameters in Table II give sufficient insight in the machine characteristics.

Using the measured currents (i_d, i_q) and the electric rotor angle γ, the inner torque was computed in real time based on [3]:

$$T_e = \frac{3}{2} p \left[(\psi_d i_q - \psi_q i_d) + \left(i_d \frac{\partial \psi_d}{\partial \gamma} + i_q \frac{\partial \psi_q}{\partial \gamma} \right) \right] \qquad (12)$$

The campbell-diagram in Fig. 8 shows a good match between calculated inner torque and measured torque. It should be noted that torque harmonics like cogging torque cannot be calculated based on flux-linkages and currents, therefore a mismatch in certain areas is expected.

Since those additional torque harmonics are usually small compared to the inner torque, the comparison gives a good indication of the measurement quality. As assumed, the torsion sensor is valid below its first resonance at approx. 830 Hz, while the acceleration sensors enable evaluation beyond its first resonance frequency at approx. 24 Hz. This allows even precise measurement of the 36th torque harmonic at 2.1 kHz.

TABLE II.   MACHINE DATA OF NANOTEC DB59M024035R [11]

Symbol	Meaning	value
P_N	Nominal power	135 W
V_N	Nominal voltage	24 V
I_N	Nominal current	8 A
p	Pole pairs	3
R_s	Stator resistance	135 mΩ
L_d	d inductance	0.2 mH
L_q	q inductance	0.2 mH
Ψ_{PM}	PM flux linkage	11.7 mVs

Since torque measurement by acceleration sensor is not possible below the first resonance frequency at 24 Hz, the two torque signals must be combined to cover the entire frequency range. This can be done either directly in the signal processing unit of the testbench or during the post-processing of the data.

A possible real time implementation is given by the *HOKA principle* [12]. In the *HOKA principle*, the signals of one
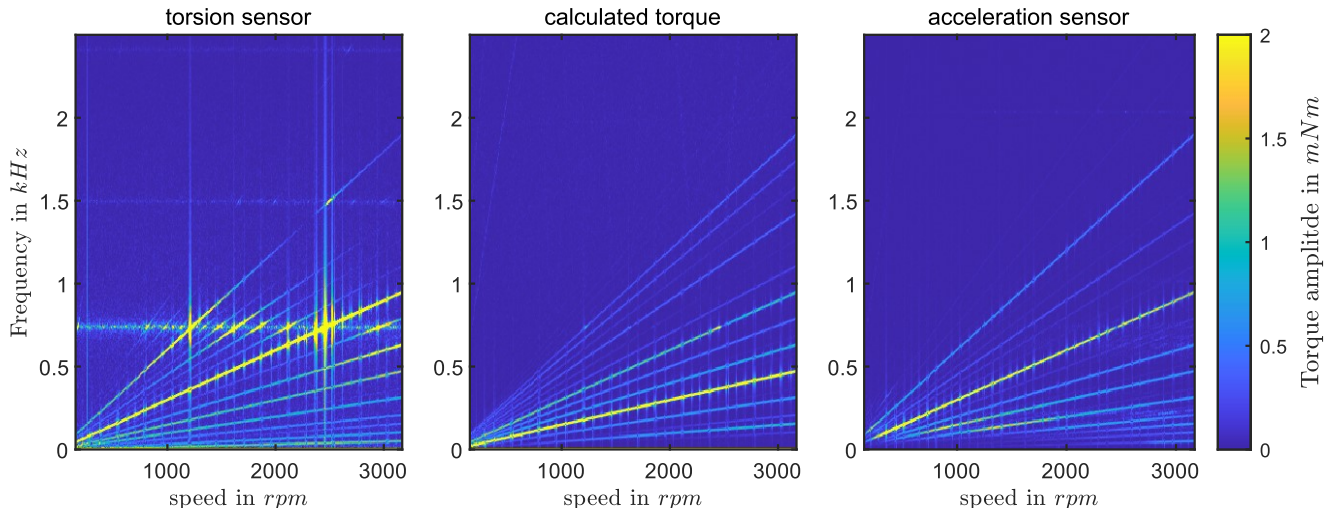
Fig. 8. Campbell-Diagram of a speed ramp from 0 to 3200 rpm. Torsion sensor setup (left), acceleration sensor setup (right) and online calculated inner torque (middle).

sensor for the low-frequency and another sensor for the high-frequency part of its measurement signal are combined by low-pass and high-pass filters. This was initially used for current measurement but can also be applied here. However, the additional phase shift of the filters causes a change in the phase angle of the respective torque harmonics depending on the rotational speed.

To avoid this, the data shown was first transformed into frequency domain in post-processing, afterwards the spectrums were combined at 250 Hz without additional filtering and smoothing.
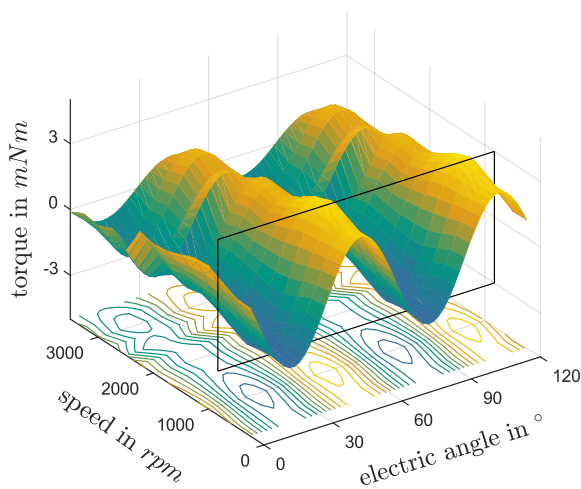
Fig. 9. Measurement of the 6th electrical order torque harmonic vs. rotational speed and electric angle.

The plot in Fig. 9 shows the 6th electric harmonic vs. rotational speeds and angle. The transition frequency is chosen to 250 Hz and indicated by the black box in Fig. 9. The maximum frequency in the graph is clearly above the resonance frequency of the torsion sensor and thus shows the performance improvement of this design compared to a conventional torque measurement setup. Furthermore, it demonstrates that there is no significant frequency dependence of the amplitude or phase of the torque measurement in this frequency range.

When using an induction motor, the proposed measurement method can also be used to obtain a characterization of individual harmonics orders across the map. This is shown in Fig. 10. Here, the DUT was operated at 700 rpm with an *EM Synergy M800006* induction motor functioning as load. The induction motors is operated at 24 V, with speeds up to 1121 rpm at 116 mNm [13].

In comparison to the hysteresis brake, torque harmonics with small amplitude are induced by the load machine, but this also allows measurement of the DUT at negative torque.

The measurement in Fig. 10 shows that even small amplitudes at high frequencies can reliably be detected by the proposed method. Even without additional filtering of the measurement results, the data shows a steady curve with low noise.
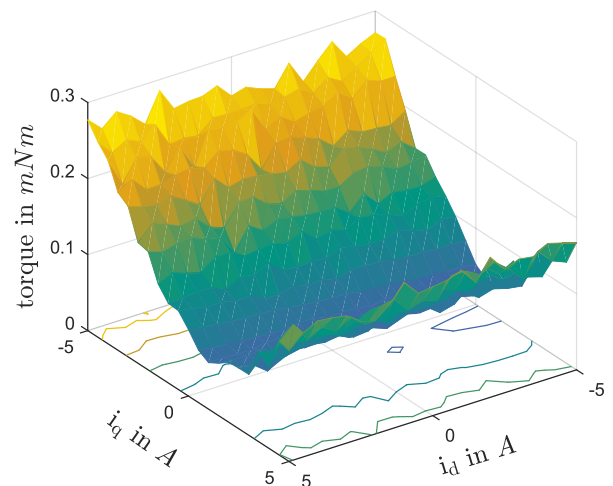
Fig. 10. Measurement of the 12th electrical order torque harmonic at 700 rpm using a induction motor as load.

As expected, the amplitude of the harmonic increases with increasing amplitudes of the q current. As shown in the measurements, there is only a slight dependence of the torque harmonic on the d current. This is due to the machine design, as the rotor is equipped with surface magnets and thus has only minimal saturation behavior.
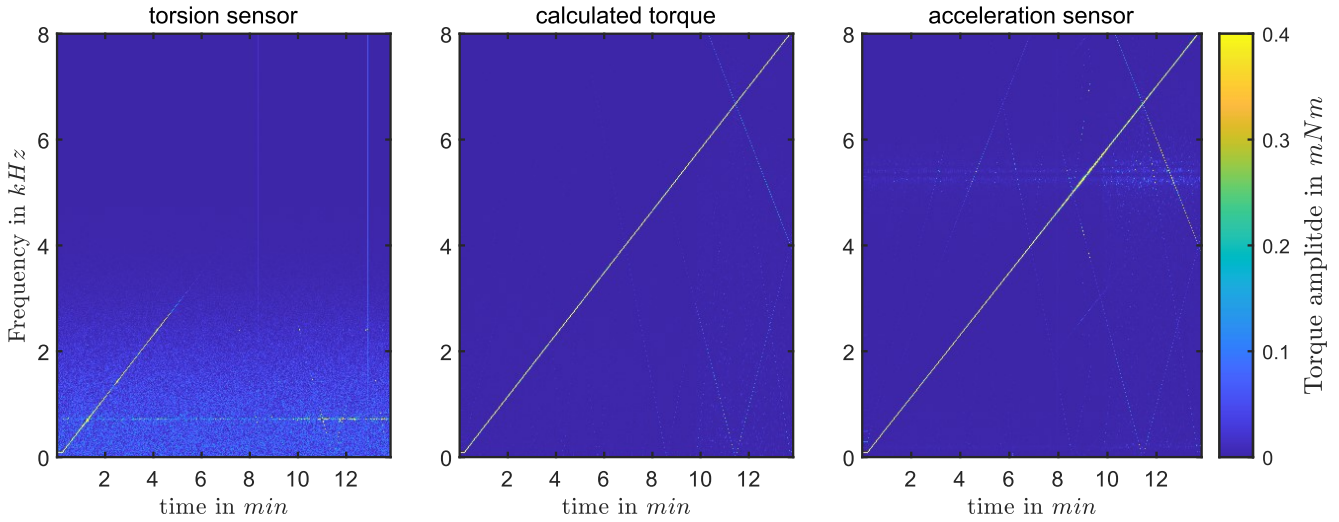
Fig. 11. Spectrogram of a linear frequency sweep from 100 Hz to 8 kHz over a period of 14 minutes. Torsion sensor setup (left), acceleration sensor setup (right) and online calculated inner torque (middle).

V. EVALUATION OF THE DESIGN

Since it has not been possible to measure the torque in this measuring range using commercial systems, the evaluation of the test bench can only be carried out using machine models. For this purpose, a three-phase sinusoidal current with an amplitude of 100 mA was injected at standstill.

The DUT was again connected to the hysteresis brake but not braked. Control was carried out by a PI current controller in the rotating reference system similar to typical machine control. In contrast to typical machine control, the transformation angle was not determined by the encoder but only from the specified setpoint frequency and angle of the three-phase system. Feedforward control and decoupling were not implemented.

The controller and switching frequency were chosen to 20 kHz. Therefore, measurements and current injection up to 10 kHz are possible but will have increased THD (total harmonic distortion) in the higher frequency range due to the discretization.

To determine the frequency dependence of the measurement system, the frequency was then increased at constant current amplitude. In contrast to the measurement shown in Fig. 8, the torque was calculated based on the average flux linkage.

This means that only the fundamental torque components were evaluated:

$$T_e = \frac{3}{2}p(\psi_d i_q - \psi_q i_d) \tag{13}$$

The spectrogram in Fig. 11 shows the online calculated torque and the measured torque by the torsion sensor and the acceleration sensors.

Due to the low shaft torque of around 4 mNm, a clear measurement noise can be seen in the measurement results of the torsion sensor. This is to be expected, as the sensor has a measuring range of 5 Nm and thus the torque to be measured is only 0.08 % of the maximum torque.

In contrast, the acceleration sensor data is almost noise-free. This is achieved by the more advantageous scaling of the high-frequency torque measurement. Since the acceleration sensors do not have to measure the fundamental shaft torque, the measuring range is shifted to smaller torques which leads to an improvement in the signal quality.
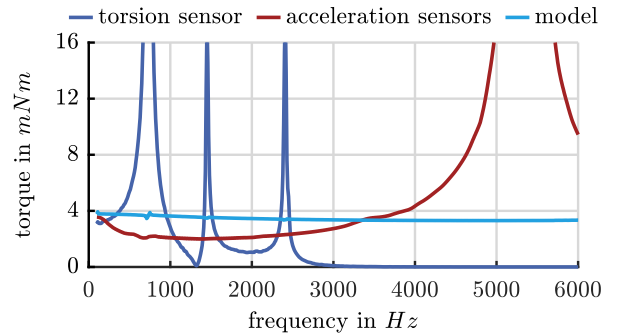
Fig. 12. Measured and calculated torque according to measurements in Fig. 11.

Fig. 12 shows the measured torque of Fig. 11. The torque over the respective frequency was obtained from the spectrogram. As expected, the resonance of the torsion sensor is clearly visible at approx. 750 Hz. This limits the measuring range upwards. In comparison, the acceleration sensors have a linear frequency response and are limited upwards by the self-resonance of the stator.

The machine model also shows a slight frequency dependence. This is due to the inferior relationship between PWM frequency and fundamental frequency, which increases the THD at higher frequencies and makes it harder to precisely adjust the fundamental amplitude. Furthermore, a small peak at approx. 750 Hz is visible, which is generated by the resonance of the torsion sensor and therefore has an influence on the current control and thus on the torque calculated by the model.

Based on the measurements, the transfer characteristics of the testbench can be calculated by:

$$G_{TS} = \frac{T_{sensor}}{T_{model}} \tag{14}$$

The characteristics are shown in Fig. 13. This demonstrates that by combining the two sensors, the measuring range can be significantly extended and improved compared to the classic measurement using a torsion shaft.

It should be noted that the transfer functions are created by comparing the inner torque of the machine with the measured torque. The influences of frequency-dependent loss components in the machine as well as non-linearities in the friction losses are neglected. Thus, it is to be expected that the real transfer function has lower frequency dependencies.
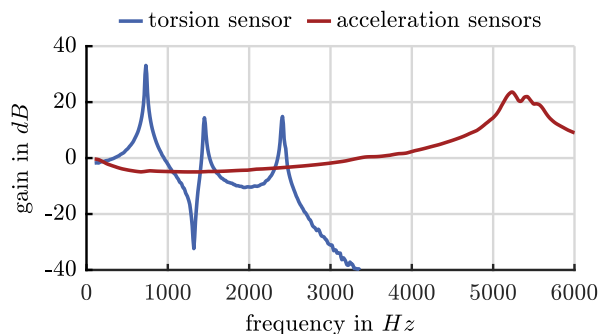
Fig. 13. Aproximated transfer behaviors of torsion and acceleration sensors by measurements and torque model for the designed testbench.

To extend the measurement accuracy and frequency range even further a frequency response correction can be implemented by means of a FIR filter or in post-processing. For this purpose, a more detailed machine model including the various non-linear loss effects must be designed or a corresponding reference measurement developed.

VI. CONCLUSIONS AND FUTURE WORK

In this paper, a new method for torque ripple evaluation with large bandwidth is presented. Compared to previous published solutions, the bandwidth was significantly increased while the complexity of wireless signal transmission and the inertia were reduced compared to the known methods. This allows a higher resolution and increases the maximum rotational speed.

Furthermore, the sensitivity and noise-level of the hybrid sensor setup were significantly improved compared to the torsion sensor. The measurements using the new method show a good alignment of the measured and predicted results.

Although the measurements have so far only been carried out on brushless dc drives, the measuring principle is not fundamentally limited to small drives and can also be used for larger drives.

VII. REFERENCES

[1] Z. Azar, Z. Q. Zhu, and G. Ombach, "Influence of Electric Loading and Magnetic Saturation on Cogging Torque, Back-EMF and Torque Ripple of PM Machines," *IEEE Trans. Magn.*, vol. 48, no. 10, pp. 2650–2658, 2012, doi: 10.1109/TMAG.2012.2201493.

[2] Y. Tadano, T. Akiyama, M. Nomura, and M. Ishida, "Periodic learning suppression control of torque ripple utilizing system identification for permanent magnet synchronous motors," in *2010 International Power Electronics Conference: IPEC-Sapporo 2010 - [ECCE Asia]; Sapporo, Japan, 21 - 24 June 2010*, Sapporo, Japan, 2010, pp. 1363–1370.

[3] S. Decker *et al.,* "Predictive Trajectory Control with Online MTPA Calculation and Minimization of the Inner Torque Ripple for Permanent-Magnet Synchronous Machines," *Energies*, vol. 13, no. 20, p. 5327, 2020, doi: 10.3390/en13205327.

[4] A. Schramm, E. Sworowski, and J. Roth-Stielow, "Methods for measuring torque ripples in electrical machines," in *2017 IEEE International Electric Machines and Drives Conference (IEMDC): 21-24 May 2017*, Miami, FL, USA, 2017, pp. 1–8.

[5] M. Martinez, D. F. Laborda, D. Reigosa, and F. Briz, "Comparative Analysis of Torque Pulsations Measurement Methods for PMSM Drives," in *2021 IEEE Energy Conversion Congress and Exposition (ECCE)*, Vancouver, BC, Canada, Oct. 2021 - Oct. 2021, pp. 5129–5135.

[6] PCB Piezotronics, Inc., *Datasheet - PCB Model 352B*. Accessed: Jun. 3, 2022[Online]. Available: https://www.pcb.com/products?m=352B

[7] Kistler Group, *Datasheet: Torque sensor 4503B*. Accessed: Jun. 8, 2022[Online]. Available: https://www.kistler.com/files/document/000-767e.pdf?callee=frontend

[8] Magtrol, *Datasheet: HB-140M-2*. Accessed: Jun. 8, 2022[Online]. Available: https://www.magtrol.com/wp-content/uploads/hb-140.pdf

[9] B. Schmitz-Rode L. Stefanski R. Schwendemann S. Decker S. Mersche P. Kiehnle P. Himmelmann A. Liske M. Hiller, "A modular signal processing platform for grid and motor control, HIL and PHIL applications," *IPEC-Himeji 2022- ECCE Asia*, 2022.

[10] J. Stoß, C. Wurster, N. Menger, M. Brodatzki, A. Liske, and M. Hiller, "Design guideline for PCB integrated, high bandwidth, current slope sensing based on a planar Rogowski coil," in *2021 23rd European Conference on Power Electronics and Applications (EPE'21 ECCE Europe)*, 2021, P.1-P.10.

[11] Nanotec, *Datasheet: DB59M024035R-B3*. Accessed: Jun. 8, 2022[Online]. Available: https://de.nanotec.com/fileadmin/files/Datenblaetter/BLDC/DB59-rund/DB59M-R/DB59M024035R-B3.pdf

[12] N. Karrer, P. Hofer-Noser, and D. Henrard, "HOKA: a new isolated current measuring principle and its features," in *Conference record of the 1999 IEEE Industry Applications Conference: Thirty-fourth IAS annual meeting, 3 - 7 October 1999, Hyatt Regency, Phoenix, Arizona, USA*, Phoenix, AZ, USA, 1999, pp. 2121–2128.

[13] Texas Instruments and EMsynergy, *Datasheet: Low Voltage AC Induction Motor*. Accessed: Jun. 8, 2022[Online]. Available: https://www.ti.com/lit/ug/spruhz8/spruhz8.pdf?ts=1654676761586